Wave Packet Calculation of Cross Sections, Product State Distributions, and Branching Ratios for the O(^{1}D) + HCl Reaction

Valentina Piermarini[†] and Gabriel G. Balint-Kurti

School of Chemistry, University of Bristol, Bristol, United Kingdom

Stephen K. Gray

Chemistry Division, Argonne National Laboratory, Argonne, Illinois 60439

Fahrettin Gögtas

Physics Department, Firat University, 23119 Elazig, Turkey

Antonio Laganà* and Marıa Luz Hernández[‡]

Dipartimento di Chimica, Università di Perugia, 06123 Perugia, Italy

Received: November 17, 2000; In Final Form: March 30, 2001

Time-dependent quantum mechanical calculations have been carried out to estimate the total reactive cross sections, product branching ratios, and product quantum state distributions for the O(^{1}D) + HCl reaction using both reactant and product Jacobi coordinates. The potential energy surface of T. Martinez et al. (*Phys. Chem. Chem. Phys.* **2000**, *2*, 589) has been used in the calculations. The theoretical predictions are compared with experimental results and with the results of classical trajectory calculations on the same surface. The comparisons demonstrate the suitability of the potential energy surface and provide useful insights into the reaction mechanism. The calculations using product Jacobi coordinates are the first calculations for this system which permit the prediction of state-to-state reaction probabilities and of product quantum state distributions.

I. Introduction

The investigation of the O(^{1}D) + HCl reaction is motivated by the importance of this process for the modeling of the chemistry of the atmosphere. Halogenated species react with O(^{1}D), which is produced by the photodissociation of O_3. OH and ClO radicals produced in this way can attack O_3 and lead to a chain of reactions removing ozone. For this reason, the O(^{1}D) + HCl system has been the subject of several studies.

Experiments include the measurement of the consumption rate of O(^{1}D),[1] the crossed beam production and detection of ClO[2] from the O(^{1}D) + HCl → ClO + H process (R1), and the laser-induced fluorescence (LIF) (including Doppler effects)[3−5] and infrared chemiluminescence[6] measurements of the vibrational distribution of the OH product resulting from the O(^{1}D) + HCl → OH + Cl reaction (R2).

Theoretical work includes ab initio calculations of points on the potential energy surface (PES)[7−11] as well as quasiclassical trajectory (QCT) runs on model[12,13] potential energy surfaces and on a PES fitted to ab initio points[11,14,15] by making use of polynomials expressed in terms of bond order (BO) coordinates.[16] These calculations were unable to reproduce all the properties derived from experimental measurements. The most successful of them were those performed on the BO PES (H1) fitted to ab initio data.[11] These were, in fact, able to reproduce all available experimental information except for the product vibrational quantum state distribution of the OH-producing channel. Recently, some new global PESs (PSB) have been developed for this system by Bowman and collaborators.[17−19] These surfaces have been used with success in quantum mechanical (QM) wave packet and QCT calculations.[19−21] Wave packet QM calculations have also been performed by Zhang and collaborators[23,24] on an old PES[12] whose asymptotes have the wrong energies relative to each other.

Another BO PES (H2)[25] has also been produced by fitting an extended set of ab initio data. This new surface is also constrained to have a more appropriate behavior in the area connecting the strong interaction region with the asymptotes and is used in the present calculations. The H2 PES features two fairly deep wells (i.e., deep with respect to asymptotic energy of the entrance channel). The deepest well is associated with the insertion of O(^{1}D) into HCl. The other well is associated with an attachment of the O atom onto the Cl end of HCl. These wells are less pronounced than those of the PSB surface. The presence of the wells and the large exothermicity of the reaction make the energy range spanned by the system quite large. Accordingly, the number of functions which must be included when expanding the system wave function is extremely large. For this reason, to carry out QM calculations, it is more convenient to use wave packet techniques based on a grid representation of the wave function. In particular, we choose to use the real wave packet (RWQM) method.[26,27] The results

[†] Permanent address: Dipartimento di Chimica, Università di Perugia, 06123 Perugia, Italy.

[‡] Permanent address: Departamento de Fısica de la Atmósfera, Universidad de Salamanca, 37008 Salamanca, Spain.

10.1021/jp004237t CCC: $20.00
Published on Web 05/30/2001

obtained are then compared with available experimental information and the result of QCT calculations.

The paper is organized as follows. In section II, we describe the salient features of the wave packet method, while some technical details and a discussion of the convergence of the calculations is given in the Appendix. Sections III−V present various aspects of our results together with comparisons with other theoretical and experimental results. Section VI presents some conclusions of the work.

II. The Real Wave Packet Approach

Quantum wave packet methods differ from the more traditional time-independent quantum approach in that they are initial value methods. That is, the calculation is started from a known quantum state of the reactants, and the solution of the time-dependent Schrödinger equation yields all possible outcomes of interest arising from this starting point. This gives the wave packet methods the great advantage of calculating state-specific reaction probabilities over the energy range of interest from a single propagation of the wave packet,[26−31] thus facilitating the calculation of several experimental properties.

In the related numerical procedure, the formalism needed for such calculations is attractively simple, and it is possible to propagate only the real part of the wave packet.[26,27] Furthermore, a particular simple damped Chebyshev iteration, as in the work of Mandelshtam and Taylor,[32,33] results if one replaces the usual time-dependent Schrödinger equation with a modified form involving the arc-cosine of the Hamiltonian operator.[26] (The same observable properties that would be obtained using the original Schrödinger equation are, of course, still obtained with this modified approach.) For the generic atom−diatom reactions

$$A + BC(v,j) \rightarrow AB(v',j') + C \quad (1)$$

$$A + BC(v,j) \rightarrow AC(v',j') + B \quad (2)$$

the state-to-state cross sections and reaction probabilities depend on the energy as well as on the initial vibrotational (v,j) state of the reactant diatomic molecule BC and on the final vibrotational (v',j') state of the product diatomic molecule AB for process 1 (or AC for process 2).

To set up the initial wave packet, we require the wave function of the overall system to be expressed in terms of the initial diatomic molecule BC wave function, $\varphi_{vj}^{BC}(r)$ (Jacobi coordinates of the reactant arrangement R, r, and Θ are used in this case). To calculate the total reactive probability and cross section, one can use reactant coordinates and analyze the wave packet along a cut corresponding to a large fixed B−C vibrational coordinate.[26,27] When the details of product properties are needed, it is more appropriate to use product coordinates. Accordingly, if reaction 1 is to be investigated, the wave packet must be analyzed in terms of the final diatomic molecule AB wave functions, $\varphi_{v'j'}^{AB}(r')$, and the primed Jacobi coordinates (R', r', and Θ') of the related arrangement channel are used. Similarly, to analyze reaction 2, the analysis is performed in terms of the final diatomic molecule AC wave functions, $\varphi_{v'j'}^{AC}(r'')$, and the double-primed Jacobi coordinates (R'', r'', and Θ'') of the related arrangement are used (in the remainder of this section, the formalism will refer only to process 1).

To start the calculations, the initial wave packet in the scattering coordinate R is built up by multiplying together a normalized Gaussian function[26] $N e^{-\alpha(R-R_0)^2}$, a phase factor of the form $e^{-ik(R-R_0)}$, which gives it a relative momentum toward the interaction region,[34] and the vibrational−rotational wave function of the diatomic reactant. The initial wave packet may therefore be written as

$$\Psi^{J\Lambda}(R,r,\Theta;t=0) = N e^{-\alpha(R-R_0)^2} e^{-ik(R-R_0)} \varphi_{vj}^{BC}(r) P_j^{\Lambda}(\Theta) \quad (3)$$

where Λ is the quantum number for the projection of the total angular momentum J on to the body-fixed z-axis, $P_j^{\Lambda}(\Theta)$ is the normalized associated Legendre polynomial, and k is the wavevector which determines the average relative momentum or kinetic energy $[E_{tr}^{\circ} = (k\hbar)^2/2\mu]$ of the collision partners. Note that in the real wave packet method only the real part of a wave packet generated by eq 3 is explicitly propagated.[26] In the following, since we mostly refer to $J = 0$ calculations, both J and Λ labels will be dropped when unnecessary.

A grid representation is used to describe the wave packet. The potential and the wave function are represented by their values on a regular grid in the scattering coordinate, R, and in the vibrational coordinate, r, and on a grid of Gauss−Legendre quadrature points in the Jacobi angle, Θ. At the initial time, the wave packet is placed in the reactant channel, and as time progresses, it moves into the interaction region. The initial wave packet is set up in reactant coordinates. If product quantum state distributions are sought, the initial wave packet is transformed into product Jacobi coordinates and the entire propagation is carried out in these coordinates. The grid must be large enough to contain the initial wave packet, the region where the analysis line is drawn, and the interaction region. It must also be fine enough to accurately describe the structure of the wave function. At the grid edges, an absorption region is introduced to prevent the wave packet amplitude from reaching the edge of the grid and causing the problem known as aliasing in Fourier transform theory.[30,31]

The real part of the wave packet is propagated in time until it has mainly been absorbed near the edge of the grid. It is analyzed at every time step along an analysis line in the asymptotic region of the product channel[26,27] so as to accumulate the data needed for the computation of the detailed **S** matrix element $S^J_{vj\Lambda,v'j'\Lambda'}(E_{tr})$ at the various values of the collision energy E_{tr} contained within the wave packet.

By summing the square modulus of the detailed **S** matrix elements over Λ and Λ', one can evaluate state-to-state reaction probabilities $P^J_{vj,v'j'}(E_{tr})$. A further summation over v' and j' leads to initial state state-selected reaction probabilities $P^J_{vj}(E_{tr})$.

Two types of wave packet calculations are reported in this paper. The first type is performed using product Jacobi coordinates. These calculations are carried out separately for the two possible reactions, R1 and R2, and have been performed for zero total angular momentum only. The advantage of these calculations is that they permit the prediction of product quantum state distributions and branching ratios. The other type of calculations is carried out using reactant Jacobi coordinates. In these calculations, the objective is to compute just the total reaction probability as a function of energy. This is done using a flux analysis method[27] in which the outgoing particle flux through a surface at fixed, moderately large values of the HCl coordinate is computed to give the desired result. This method has been skillfully adapted in the work of Christoffel et al.[20] to permit the prediction of branching ratios, but this approach has not been used in the paper presented here. The calculations using reactant Jacobi coordinates are performed for many values of the total angular momentum, J, using a helicity-decoupled approach, and the results are used to compute approximate total reactive cross sections.

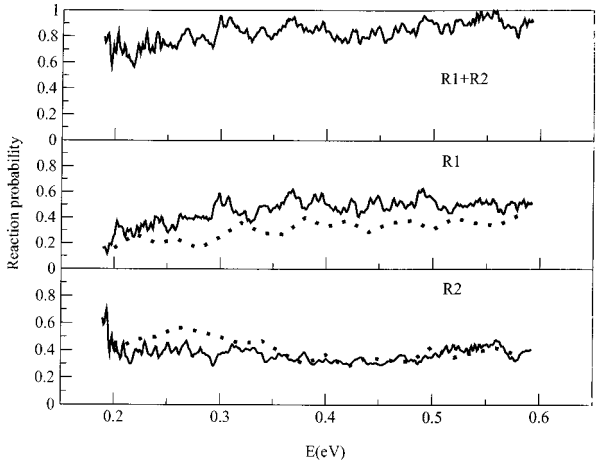

Figure 1. Total reaction probabilities out of the $v = 0$, $j = 0$ initial state plotted vs total energy E. The calculations were performed using product Jacobi coordinates and the real wave packet quantum mechanical method with zero total angular momentum: (upper panel) summed over R1 and R2 channels, (middle panel) R1 channel, and (lower panel) R2 channel. For comparison, values obtained by Christoffel et al.[20] are shown as dotted lines. These values were estimated from Figure 2 of ref 20.

III. Reaction Probabilities

Quantum real wave packet calculations were performed for the reactions

$$O(^1D) + HCl(v,j) \rightarrow ClO(v',j') + H \qquad (R1)$$

and

$$O(^1D) + HCl(v,j) \rightarrow OH(v',j') + Cl \qquad (R2)$$

on the H2 surface. Reactants were started in their lowest vibrational and rotational states ($v = 0, j = 0$). Each wave packet calculation yields results for a range of energies. In the calculations presented here, this range was typically ~0.4 eV. The range is centered around the translational energy, $E_{tr}^{\circ} = (k\hbar)^2/2\mu$ (see eq 3), chosen for the wave packet in the reactant channel. For the calculations reported here, E_{tr}° was chosen to be between 0.02 and 0.35 eV. This provided reaction probabilities over a translational energy range up to 0.52. Details of the wave packet calculations, such as grid sizes, absorption parameters, etc., and discussion of convergence tests are given in the Appendix. In some cases, more than one calculation was performed using different values of E_{tr}° so as to fully cover the energy range of interest.

We consider first the total reactive probability $P_{v=0,j=0}(E_{tr})$ summed over all product states and product channels (R1 and R2). This quantity is shown as a solid line in the upper panel of Figure 1. The curves shown in the figure have been computed using product Jacobi coordinates and zero total angular momentum. All the reaction probabilities, including the total reaction probability $P_{v=0,j=0}(E_{tr})$, show a sharp rise at threshold, at $E \sim 0.186$ eV, which corresponds to zero translational energy. In common with many previous time-dependent reactive scattering calculations, the results close to this threshold region are considered unreliable and display a sharp peak, which has been omitted from the figure.[34] As the energy increases, the average value of the initial state-selected total reaction probability remains substantially constant, while its actual value shows a dense structure of peaks. Calculations using reactant Jacobi coordinates lead to very similar curves.

In the central panel of Figure 1, we plot as a solid line the state-selected $P_{v=0,j=0}$ total reactive probability for reaction R1 (producing ClO products) and, in the bottom panel, that for reaction R2 (producing OH products). As is apparent from the figure, the probability for R2 calculated on the H2 potential (solid line of the lower panel) shows a sudden rise at threshold similar to that of the total reactive probability of the upper panel. In this case, however, the maximum is followed by a substantial decrease at larger energies. For even larger energies, it stabilizes to a value of ~0.4. The corresponding probability for R1 (solid line of the central panel) rises sharply at threshold to a value of ~0.2 and then increases more smoothly to a maximum of ~0.6 (around 0.42 eV), after which it gradually decreases. This suggests a different mechanism for the two reaction channels.

QCT studies have already highlighted important features of the reaction dynamics of the $O(^1D)$ + HCl reaction.[25] Of key importance is the fact that all trajectories explore at least one of the wells, though for less than a complete rotation. Therefore, even if the action of the wells is unable to enforce a statistical behavior, it is a useful paradigm for classifying the reactive approach either as attachment (when O attacks on the Cl side) or as insertion. As a matter of fact, at the energy of the crossed beam experiment,[2] one-third of the trajectories react via attachment (shorter-lived) and two-thirds by insertion (longer-lived). If the impact parameter b, instead of time, is monitored, other important features of the reaction mechanism are singled out. For both R1 and R2 reactions, attachment processes lead to the usual "hard-sphere like" shape (an opacity function which is nearly constant for small b values and rapidly decreases to zero at higher b values). In contrast, while insertion processes leading to ClO still show the same type of opacity function as attachment processes, the ones associated with the formation of OH show an opacity function exhibiting the less common feature of having a maximum at a large impact parameter.[15,25] This is a sign of the high reactivity of H on the H2 PES when attack does not occur on the Cl end, and this is in accord with the substantially heavy heavy light (HHL) nature of R1 as opposed to the substantially heavy light heavy (HLH) nature of R2.

The reaction probability for reaction R2 using the H2 PES, given as a solid line in the lower panel of Figure 1, may be compared with that calculated using the PSB PES,[20] which are plotted as dots and with those reported by Bitterova et al. in ref 19. We see that our calculations predict a sharp rise in the reaction probability at threshold followed by a decrease for the H2 PES. This is characteristic of a barrierless reaction and agrees well with the results reported in Figure 2 of ref 19. Our analysis of Figure 2 of ref 20, in which an older version of the PSB potential was used, shows a different form for the threshold behavior of the OH + Cl (R2) channel. Note that there is in fact a small barrier to reaction on the H2 surface. There is also a strong likelihood that tunneling makes a substantial contribution to the computed reaction probability near threshold. For reaction channel R1, the probability increases more gradually above threshold, implying a less effective contribution of tunneling to this reactive process. This behavior is also observed on the PSB surface.[19,20] The possibility of large contributions of tunneling to reaction for processes involving the exchange of H with respect to the exchange of heavier atoms (Cl in our case) is nicely exemplified in the study of the F + HD and F + DH reactive processes of ref 35. Attention should also be drawn to the comparison of quantum and classical trajectory calculations presented in Figure 2 of ref 20. This figure illustrates the general good agreement between classical trajectory and quantum results and indicates that the contribution of

tunneling to the reaction probability in the threshold region should be rigorously examined.

The reactive probability versus energy plots of Figure 1 exhibit a dense structure of peaks that is similar to both the results of Bowman and collaborators calculated on the original PSB surface (results plotted here as dots are interpolated from those shown in Figure 2 of ref 20) and the results calculated using their new improved surface (see ref 19). Our results do not differ substantially from those given by Bowman and collaborators:[19,20] the global reactive probability rises sharply at threshold and then stabilizes at higher energies. As already mentioned, the largest overall difference between the results for the H2 and PSB surfaces occurs for reaction R1. In this case, reaction probabilities calculated using the PSB surface are always lower than those calculated using the H2 surface, with the deviation varying from 0.1 to 0.2. The overall agreement of PSB and H2 results for R2 is definitely better.

IV. Branching Ratio and Cross Sections

The ratio of the two probabilities $P^{R1}_{v=0,j=0}/P^{R2}_{v=0,j=0}$ for zero total angular momentum can provide an approximate estimate of the branching ratio between the R1 and R2 reactions. This value varies from 0.3 in the immediate vicinity of the threshold to about 1.25 at the higher end of the energy interval that is considered. For probabilities calculated on the PSB surface, this ratio varies approximately in the same range (values of ref 20) or is approximately constant around 0.3 (values of ref 19). All these values agree with the experimental information of ref 2 that gives a lower limit of 0.34 ± 0.10 for the branching ratio at $E_{tr} = 0.33$ eV.

A proper theoretical estimate of the branching ratio requires the calculation of the cross sections for both R1 and R2 processes. If performed exactly, this calculation would require the integration of the quantum mechanical scattering equations for all the contributing initial vibrational, rotational, and total angular momentum quantum numbers. This is still a difficult computational task. For this reason, some simplifications have been introduced.

QCT calculations indicate that for low reactant rotational states the reaction probability is similar to that for $j = 0$ (as implied also by the QM wave packet calculations of ref 19). We consider here only contributions from the ground rotational state.

To estimate reliably the total (R1 + R2) reactive cross section from the initial reactant state ($v = 0$, $j = 0$), calculations for the total reaction probability were performed for a large number of non-zero values of the total angular momentum quantum number, J. These calculations were performed in reactant Jacobi coordinates for J values of 0, 1, 2, 5, 10, 20, 50, 75, 100, 130, 150, and 160 using a helicity-decoupling approximation (i.e., Λ is assumed to equal zero throughout).[36] The reaction probabilities calculated in this way are shown in Figure 2 for J values of 0, 50, 100, and 130. The figure is similar in all qualitative respects to Figure 4 of Lin et al.[23] Two key features which should be noted from the figure are that, as expected, the threshold for reaction increases with increasing total angular momentum and that the reaction probability, in the high-energy limit, decreases with increasing J. The $J = 0$ line in Figure 2 may be compared with the top panel of Figure 1. The graphs are similar but differ in the positioning of the detailed oscillations. Very many calculations of increasing size have been performed to obtain fully converged results for calculations using both reactant and product coordinates. The convergence issues are discussed in the Appendix. While there clearly remain some aspects of the calculations which are not absolutely converged, all physical quantities reported are stable and are not significantly changed by improving the calculations, i.e., by increasing the number of grid points, etc. The integral cross section may be written as

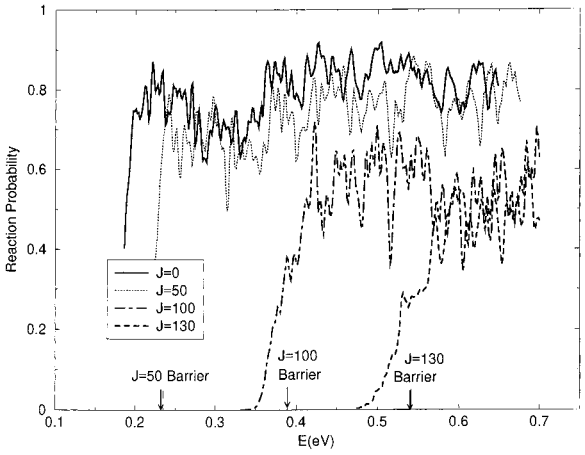

Figure 2. Total reaction probabilities out of the $v = 0$, $j = 0$ initial state plotted vs total energy E for four different total angular momenta, J. The calculations were performed using reactant Jacobi coordinates and the real wave packet quantum mechanical method.

$$\sigma(E_{tr}) = \frac{\pi}{k_{vj}^2}\sum_{J=0}^{\infty}(2J+1)P^J_{v=0,j=0}(E_{tr}) \qquad (4)$$

From the equations, we see that we need the reaction probability for all values of J for which it is non-zero at the energy of interest. For some values of J, we have this quantity from our quantum calculations. Approximate J-shifting[37,39,40] and related capture model methods[36] have been developed to estimate the required reaction probabilities for those values of J for which actual calculations have not been performed, from probabilities for J values for which they are available. The capture model methods were developed to treat situations for which there is no barrier to reaction. In the present case, the threshold to reaction occurs at zero translational energy, indicating that there is no effective barrier to reaction, and we therefore use a modified capture model method to estimate the total reactive cross section.

In the capture model, for a value of J for which we need to estimate the reaction probability, we replace $P^J_{v=0,j=0}(E_{tr})$ in eq 4 with $P^{\bar{J}}(E_{tr}-E^{J\bar{J}}_{tr})$, where $P^{\bar{J}}(E_{tr}-E^{J\bar{J}}_{tr})$ is the reaction probability from the nearest, lower-lying $\bar{J}$ value for which we have performed quantum calculations. The probability curve for this $\bar{J}$ value is shifted down in energy by an amount $E^{J\bar{J}}_{tr}$ which is the difference in the height of the centrifugal barrier for J and $\bar{J}$ (the J value for which we have actually performed the quantum calculations). The centrifugal barrier is estimated using an effective potential which is derived by taking the expectation value of the potential over the vibrational−rotational state of the reactant diatomic molecule in its initial vibrotational state. In Figure 2, the arrows on the x-axis indicate the energies of the barriers on the $J = 50$, 100, and 130 effective potentials. It is very noticeable that for all the larger angular momenta there is a substantial reaction probability at energies lower than these barriers. This indicates that a reorientation effect, or possibly tunneling, is present in the reaction dynamics.

The probabilities shown in Figure 2 clearly demonstrate that standard J-shifting[37,39,40] or capture[36] models will not work for

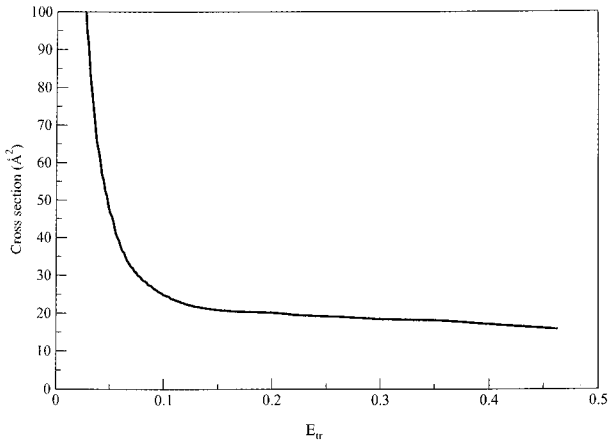

Figure 3. Total reactive cross section calculated using a modified capture model plotted as a function of collision energy E_{tr}.

this case. This is because not only is the reaction probability shifted to higher energies with increasing total angular momentum, but its magnitude is also decreased. Bittererova et al.[19] have elegantly analyzed this problem and have developed a sophisticated, but difficult to use, new *J*-shifting procedure.[38] Our approach to this problem has been first to compute the reaction probabilities for a large set of total angular momentum values (*J* values) spanning nearly the entire range which contributes to the reaction cross section. This is up to 175 for the energies we consider. If we then need the reaction probability for a *J* value between two *J* values (J_1 and J_2) for which we have already computed the exact reaction probabilities, we proceed as follows.

(1) Use the capture model to estimate $P^J(E_{tr})$ starting from the lower of the two total angular momenta J_1. This gives us $P^J(E_{tr}-E_{tr}^{J_1J})$.

(2) Use the capture model to estimate the same quantity, but now starting from the reaction probability calculated using J_2. This gives us $P^J(E_{tr}-E_{tr}^{J_2J})$ (note that $E_{tr}^{J_2J}$ is negative).

(3) Now estimate the reaction probability for total angular momentum *J*, $P^J(E_{tr})$, by interpolating between these two estimates:

$$P^J(E_{tr}) = P^J(E_{tr}-E_{tr}^{J_1J})\left(\frac{J_2-J}{J_2-J_1}\right) + P^J(E_{tr}-E_{tr}^{J_2J})\left(\frac{J-J_1}{J_2-J_1}\right) \quad (5)$$

This procedure is in fact the same as that used by Gray et al.[41]

The estimated total reaction cross section is shown in Figure 3. These results may be compared with the most recent results of the Bowman group (Figure 11 of ref 19). The total reactive cross sections predicted using the H2 surface (i.e., the calculations presented here) are clearly larger, by a factor of ~1.8, than those computed using the improved PSB potential. This does not arise from significantly greater reaction probabilities for a particular value of *J* but must rather arise from a larger range of *J* values contributing to the cross section (see eq 4).

V. Product Distributions

Additional indications concerning the suitability of the proposed PES are provided by a comparison of calculated energetic distributions of the products with experimental data. Information about the product vibrational distribution (PVD) of R2 comes from the infrared chemiluminescence experiment[6] already mentioned. To better understand the main features of the PVDs, these were calculated for both R1 and R2 processes at different translational energy values. Some of these distributions are shown in Figure 4, after normalization to a maximum value of 1.0.

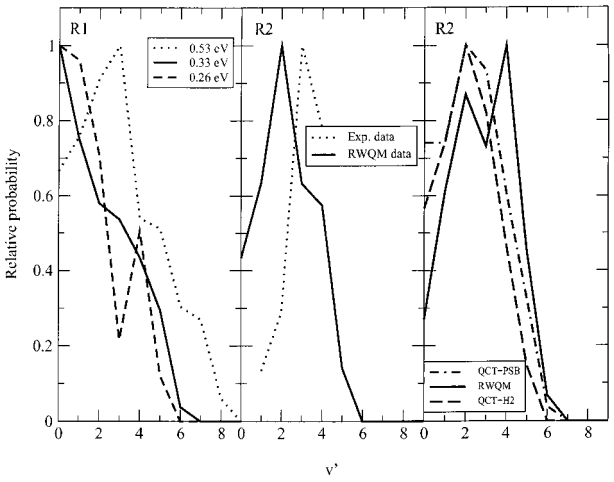

Figure 4. Normalized product vibrational distributions. In the middle panel are shown RWQM H2 (—) OH product vibrational state distributions calculated at a collision energy of 0.26 eV for reactants initially in their lowest vibrational−rotational state. For comparison, experimental data[6] (•••) are also shown. In the right-hand panel are shown RWQM H2 (—), QCT H2 (− − −), and QCT PSB (•−−•)[20] OH product vibrational state distributions calculated at a collision energy of 0.53 eV. In the left-hand panel are shown QCT H2 OCl product vibrational state distributions calculated at a collision energy of 0.26 (− − −), 0.33 (—), and 0.53 eV (•••).

The central panel of Figure 4 compares the PVD calculated at $E_{tr} = 0.26$ eV using the real wave packet quantum mechanical (RWQM) method with the experimentally determined quantity measured for collision energies ranging from 0 to 0.26 eV.[6] Both distributions are normalized to unity at their maximum value. The calculated and experimental PVDs agree fairly well, both being inverted with the RWQM distribution peaking at $v' = 2$, one vibrational quantum less than the measured one. QCT results have not been published at 0.26 eV. However, as shown in the right-hand panel of the figure, where the various PVDs calculated on both H2 and PSB PESs for R2 at 0.53 eV are plotted, the two quasiclassical results are substantially identical since they both peak at $v' = 2$ (with $v' = 3$ being the next more populate state) and die off at $v' = 6$. In contrast, the RWQM PVD is clearly much hotter since it has an absolute maximum at $v' = 4$ and a secondary one at $v' = 2$. The inversion of the PVD for OH is made stronger by an increase in the collision energy. The same is true for the transfer of Cl. For this process, as shown in the left-hand panel of the same figure, the maximum of the calculated PVD gradually shifts from $v' = 0$ to $v' = 3$ as the energy increases from 0.26 to 0.53 eV.

A further comparison with the experiment can be carried out in terms of the translational energy distribution of the products. The product translational distribution (PTD) for the ClO-forming process was derived from the measurements of ref 2. In the left-hand panel of Figure 5, we compare the PTD for R1 calculated using the RWQM method with a *J* of 0 at $E_{tr} = 0.53$ eV on the H2 surface with the QCT ones obtained on both H2 (− − −) and PSB (−••−), and experimental information (•••). To make the comparison more homogeneous, we have boxed RWQM results that are by nature discrete (boxes of size 0.22 and 0.05 eV were used for OH and ClO, respectively). Again, the agreement between QCT results obtained on the two surfaces is fairly good, and the agreement with experimental data is also excellent. The agreement with the RWQM PTD is on the average fairly good. A peculiarity of the quantum PTD is the structure that reflects the product vibrational state distribution

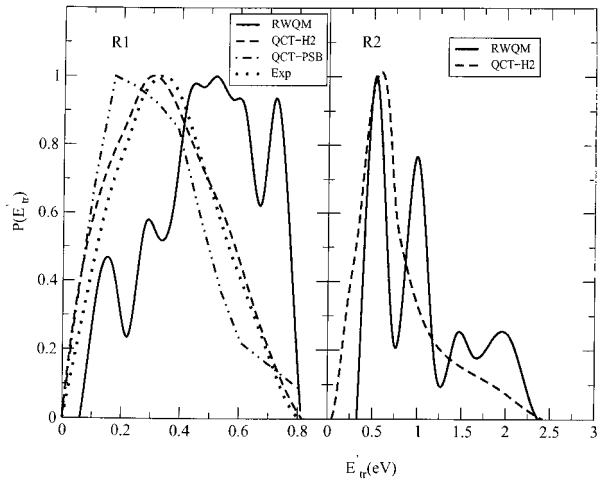

Figure 5. Product translational distributions calculated at $v = j = 0$ and a collision energy of 12.2 kcal/mol. In the left-hand panel are shown RWQM H2 (—), QCT H2 (− − −), QCT PSB (−••−), and measured (•••) distributions for R1. In the right-hand panel are shown RWQM H2 (—) and QCT H2 (− − −) distributions.

with which it is associated. A finer resolution of measured data could, possibly, improve the quality of the comparison.

In the right-hand panel of the Figure 5, PTDs which were calculated using QCT and RWQM methods on the H2 potential energy surface for the OH + Cl channel (R2) are presented. Apart for the fine structure of the quantum distribution, the agreement between the QCT and RWQM results is also satisfactory in this case. It should be remembered that the quantum mechanical calculations are performed for zero total angular momentum and for reactants in their lowest vibrational−rotational state. In contrast, the QCT calculations include all total angular momenta and sample a thermal distribution of initial quantum states. This means that it is not really possible to make detailed comparisons between these two types of calculations.

VI. Conclusions

Time-dependent quantum calculations performed on the H2 PES suggest that the quantum contribution to reactivity at threshold may be important. As a matter of fact, the energy dependence of the total reaction probability for both reactive processes has a negative slope at (or maybe just marginally above) threshold. Reaction R2 has a higher probability at threshold, and this may arise from a tunneling contribution at these low energies.

The reaction probabilities which result directly from the quantum mechanical calculations are not experimentally measurable. To make predictions about the total reactive cross section, which is an observable quantity, quantum mechanical reactive scattering calculations were performed using reactant Jacobi coordinates within the helicity decoupling approximation for a wide range of total angular momenta ($J = 0$, 1, 2, 5, 10, 20, 50, 75, 100, 130, 150, and 160). These calculations have enabled us to reliably predict the total reactive cross section as a function of collision energy.

In this paper, we have presented the first state-to-state quantum reactive scattering calculations for the O(^{1}D) + HCl system. These were performed using product Jacobi coordinates and have permitted us to make predictions about product quantum state distributions for the system. Product vibrational state and translational energy distributions, whose detailed nature is a critical test of the accuracy of the PES, show that quantum effects are important for these reactions, showing significant differences between QCT and QM results. In particular, we found that QCT results obtained on two different PESs lead to substantially identical vibrational distributions. On both surfaces when moving to higher energies, these distributions become broader and shift their maximum to higher vibrational quantum numbers. However, QM distributions always have a peak displaced to a higher quantum number.

TABLE 1: Grid and Initial Condition Details for Wavepacket Calculations Using OH−Cl and OCl−H Product Jacobi Coordinates[a]

	OH−Cl	OCl−H
scattering coordinate (R') range/a_0	0−15	0−15
no. of grid points in R'	251	251
internal coordinate (r') range/a_0	0−12	0−14
no. of grid points in r'	251	229
no. of angular grid points	94	100
absorption region length in R' (r')/a_0	4(2)	4(4)
absorption strength (c_{abs})[b]	0.1	0.1
center of initial (sinc) wave packet[34] (R_0)/a_0	7	7
width of the wave packet, α	8.0	8.0
smoothing of the wave packet, β	0.2	0.2
initial translational energy, E_{tr} (eV)	0.08, 0.35	0.08, 0.35
position of analysis line, R_∞'	10	10

[a] All quantities are given in atomic units. [b] The damping operator $\hat{A}$ used corresponded to an exponential imaginary absorbing potential. See appendix for details.

Acknowledgment. Thanks are due to the EU COST program in chemistry, action D9, for supporting a stay of V.P. at Bristol within the short term mobility program. Financial support from MURST, ASI, and CNR is also acknowledged. We thank the EPSRC for the provision of funds to purchase the computers on which this work was performed and for funds to underpin the collaboration under the COST program. S.K.G. was supported by the Office of Basic Energy Sciences, Division of Chemical Sciences, U.S. Department of Energy, under Contract W-31-109-ENG-38. F.G. thanks TUBITAK for financial support via Grant 1739. M.L.H. thanks DGESIC of Spain for financial support (Grant PB98-0281).

Appendix

Details of Quantum Wave Packet Calculations and Discussion of Convergence. In this Appendix, details of the wave packet calculations are presented and a discussion of the convergence of the results is given. Three types of wave packet calculations were performed to obtain the results presented in the body of the paper. These were (1) calculations using OH−Cl product Jacobi coordinates; (2) calculations using OCl−H product Jacobi coordinates, and (3) calculations using O−HCl reactant Jacobi coordinates.

The details of the calculations using OH−Cl and OCl−H product Jacobi coordinates are presented in Table 1. The damping operator,[26] $\hat{A}$, used for the product coordinate calculations corresponds to an exponential imaginary absorbing potential.[34,42,43] The detailed form of the operator is $A_x(x) = \exp\{-c_{abs} \exp[-2(x_{max} - x_{abs})/(x - x_{abs})]\}$ for $x > x_{abs}$ and $A_x = 1$, and otherwise for $x = R'$ or r'. The calculations were entirely "grid-based". This means that the wave packet was represented on an angular grid based on Gauss−Legendre quadrature points[44,45] and the effective number of angular basis functions is equal to the number of angular quadrature points. The state-to-state reaction probabilities are obtained by analyzing the wave packet at each time step[26] along a cut at a large fixed value of the product scattering coordinate, R_∞'.

TABLE 2: Grid and Initial Condition Details for Wavepacket Calculations Using O−HCl Reactant Jacobi Coordinates[a]

scattering coordinate (R) range/a_0	0−14
no. of grid points in R	251
internal coordinate (r) range/a_0	0−11.5
no. of grid points in r	251
no. of angular grid points	127
absorption region length in R (r)/a_0	4(4)
absorption strength (c_{abs})[b]	0.005
center of initial (sinc) wave packet[34] (R_0)/a_0	9.5
width of the wave packet, α	0.4
initial translational energy, E_{tr} (eV)	0.08, 0.35
position of analysis line, r_∞	6

[a] All quantities are given in atomic units. [b] The damping operator, $\hat{A}$, used corresponded to a quadratic imaginary absorbing potential. See the Appendix for details.

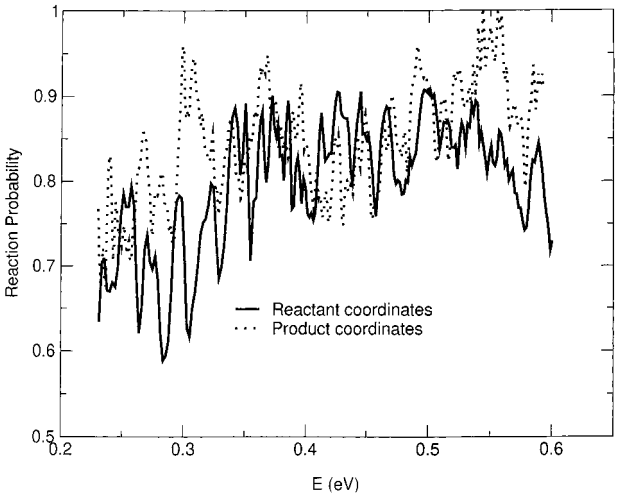

Figure 6. Comparison of total reaction probability computed using reactant (—) and product (···) Jacobi coordinates.

The details of the calculations using O−HCl reactant Jacobi coordinates are presented in Table 2. The damping operator,[26] $\hat{A}$, used for these calculations corresponds to a quadratic imaginary absorption potential.[42,43] For the calculations using reactant coordinates, our interest is in the total reaction probability for each value of J that is used. For these calculations, we have used a flux analysis method,[27] and the analysis line was located at a large fixed value of the H−Cl vibrational coordinate. For the reactant coordinate calculations, the computer code used angular basis functions, rather than grid points, as the primary representation.

Each wave packet calculation in product coordinates typically takes more than 1 week to complete on our SGI/R10000 Origin 200 computer, while those using reactant coordinates take ∼2 days. Very many test calculations have been carried out, spanning a period of more than 1 year, to test and confirm the results reported in the paper.

Figure 6 compares the total reaction probability for a J of 0 calculated using reactant and product coordinates. The total reaction probability calculated using product reaction coordinates is in fact the sum of two independently computed reaction probabilities, one for the OH + Cl product and one for the OCl + H product. The agreement between reaction probabilities calculated using reactant and product coordinates is not nearly as good as that which has been obtained for the O + H_2 system.[34] This reflects the greater difficulty of performing quantum mechanical calculations on systems containing heavy nuclei. The cross section for the reaction is the result of summing over reaction probabilities for many J values (see eq 4). The result of this can be seen in Figure 3, where the result of summing over many J values has completely smoothed out the original oscillations in the reaction probabilities. The most important aspect of the reaction probabilities as far as the reactive cross sections are concerned is therefore the average value of the reaction probability over a range of energies, rather than the detailed oscillation which the reaction probability displays on a fine energy scale. The average of the product coordinate total reaction probability over the energy range of 0.23−0.6 eV is 0.845, while the same average for the reactant coordinate calculations is 0.804. The difference in the average reaction probabilities over the range of the calculations is 5%, and this represents a fair assessment of the uncertainty in the results presented here.

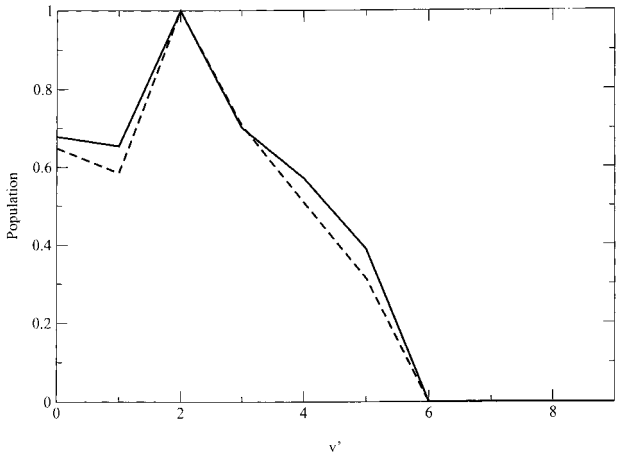

Figure 7. Comparison of OH product vibrational distributions using results of two different product Jacobi coordinate calculations. The two calculations used different numbers of angular basis functions: (—) 94 angular basis functions and (− − −) 80 angular basis functions.

We note that these are the very first calculations presented for the system in which product Jacobi coordinates have been used, and therefore also the first calculations which have been able to address the product quantum state distribution in the reaction. No comparisons of the type we present here have before been possible for this system. Our reactant coordinate calculations are similar in specification to those used in some other publications.[20] Lin et al.[23] however have used a far larger number of angular basis functions. We have performed calculations with up to 120 angular basis functions to check the results presented here. Such calculations result in changes to the detailed fine structure in the reaction probability versus energy graphs, but they do not significantly change the average value of the reaction probability, which is the essential quantity which determines the observable quantity, namely, the total reaction cross section.

The question of the reliability of the product quantum state distributions predicted by our calculations then arises. In an attempt to examine this question, we have computed OH product vibrational quantum state distributions from two independent wave packet calculations which used different numbers of angular basis functions, 80 and 94. The results are shown in Figure 7. The maximum difference between the two sets of product state distributions is 5%, confirming our previous estimate of the reliability of our results.

References and Notes

(1) Wine, P. H.; Wells, J. K.; Ravishankara, A. R. *J. Chem. Phys.* **1986**, *84*, 1349.

(2) Balucani, N.; Beneventi, L.; Casavecchia, P.; Volpi, G. G. *Chem. Phys. Lett.* **1991**, *180*, 34.

(3) Lunts, A. C. *J. Chem. Phys.* **1980**, *73*, 5393.
(4) Park, C. R.; Wiesenfeld, J. R. *Chem. Phys. Lett.* **1989**, *163*, 230.
(5) Alexander, A. J.; Brouard, M.; Rayner, S. P.; Simons, J. P. *J. Chem. Phys.* **1996**, *207*, 215.
(6) Kruus, E. J.; Niefer, B. I.; Sloan, J. J. *Chem. Phys.* **1988**, *88*, 985.
(7) Bruna, P. J.; Hirsch, G.; Peyerimhoff, S. D.; Buenker, R. *Can. J. Chem.* **1979**, *57*, 1839.
(8) Escribano, R. M.; Di Lonardo, G.; Fusina, L. *Chem. Phys. Lett.* **1996**, *259*, 614.
(9) Mirri, A. M.; Scappini, F.; Cazzoli, G. *J. Mol. Spectrosc.* **1971**, *111*, 157.
(10) Turner, A. G. *Inorg. Chim. Acta* **1986**, *38*, 218.
(11) Hernández, M. L.; Redondo, C.; Laganà, A.; Ochoa de Aspuru, G.; Rosi, M.; Sgamellotti, A. *J. Chem. Phys.* **1996**, *105*, 2710.
(12) Schinke, R. *J. Chem. Phys.* **1984**, *80*, 5510.
(13) Laganà, A.; Ochoa de Aspuru, G.; Garcia, E. *J. Phys. Chem.* **1995**, *99*, 3886.
(14) Alvariño, J. M.; Bolloni, A.; Hernández, M. L.; Laganà, A. *J. Phys. Chem. A* **1998**, *102*, 10199.
(15) Alvariño, J. M.; Hernández, M. L.; Laganà, A.; Rodriguez, A. *Chem. Phys. Lett.* **1999**, *313*, 299.
(16) Garcia, E.; Laganà, A. *Mol. Phys.* **1985**, *56*, 629.
(17) Skokov, S.; Bowman, J. M.; Peterson, K. A. *J. Chem. Phys.* **1998**, *109*, 2662.
(18) Peterson, K. A.; Skokov, S.; Bowman, J. M. *J. Chem. Phys.* **1999**, *111*, 2445.
(19) Bittererova, M.; Bowman, J. M.; Peterson, K. A. *J. Chem. Phys.* **2000**, *113*, 6186.
(20) Christoffel, K. M.; Kim, Y.; Skokov, S.; Bowman, J. M.; Gray, S. K. *Chem. Phys. Lett.* **1999**, *315*, 275.
(21) Bittererova, M.; Bowman, J. M. *J. Chem. Phys.* **2000**, *113*, 1.
(22) Matsumi, Y.; Tonokura, K.; Kawasaki, M.; Tsuji, K.; Obi, K. *J. Chem. Phys.* **1993**, *98*, 8330.
(23) Lin, S. Y.; Han, K. L.; Zhang, J. Z. H. *Phys. Chem. Chem. Phys.* **2000**, *2*, 2529.
(24) Lin, S. Y.; Han, K. L.; Zhang, J. Z. H. *Chem. Phys. Lett.* **2000**, *324*, 122.
(25) Martinez, T.; Hernández, M. L.; Alvariño, J. M.; Laganà, A.; Aoiz, F. J.; Menendez, M.; Verdasco, E. *Phys. Chem. Chem. Phys.* **2000**, *2*, 589.
(26) Gray, S. K.; Balint-Kurti, G. G. *J. Chem. Phys.* **1998**, *108*, 950.
(27) Meijer, A. J. H. M.; Goldfield, E. M.; Gray, S. K.; Balint-Kurti, G. G. *Chem. Phys. Lett.* **1998**, *293*, 270.
(28) Balint-Kurti, G. G.; Gögtas, F.; Mort, S. P.; Offer, A. R.; Lagana, A.; Gervasi, O. *J. Chem. Phys.* **1993**, *99*, 9567.
(29) Gögtas, F.; Balint-Kurti, G. G.; Offer, A. R. *J. Chem. Phys.* **1996**, *104*, 7927.
(30) Balint-Kurti, G. G. In *Lecture Notes in Chemistry*; Laganà, A., Riganelli, A., Eds.; Springer-Verlag: New York, 2000; Vol. 75, p 74.
(31) Piermarini, V.; Hankel, M. In *Lecture Notes in Chemistry*; Laganà, A., Riganelli, A., Eds.; Springer-Verlag: New York, 2000; Vol. 75, p 209.
(32) Mandelshtam, V. A.; Taylor, H. S. *J. Chem. Phys.* **1995**, *102*, 7390.
(33) Mandelshtam, V. A.; Taylor, H. S. *J. Chem. Phys.* **1995**, *103*, 2903.
(34) Note that for the calculations using product Jacobi coordinates a sinc wave packet was used. See: Hankel, M.; Balint-Kurti, G. G.; Gray, S. K. *J. Chem. Phys.* **2000**, *113*, 9658.
(35) Skodje, R. T.; Skouteris, D.; Manolopoulos, D. E.; Lee, S.-H.; Dong, F.; Liu, K. *J. Chem. Phys.* **2000**, *112*, 4536.
(36) Gray, S. K.; Goldfield, E. M.; Schatz, G. C.; Balint-Kurti, G. G. *Phys. Chem. Chem. Phys.* **1999**, *1*, 1141.
(37) Sun, Q.; Bowman, J. M.; Schatz, G. C.; Sharpe, J. R.; Connor, J. N. L. *J. Chem. Phys.* **1990**, *92*, 1677.
(38) Balint-Kurti, G. G. In *Lecture Notes in Chemistry*; Laganà, A., Riganelli, A., Eds.; Springer-Verlag: New York, 2000; Vol. 75, p 101.
(39) Bowman, J. M. *J. Phys. Chem.* **1991**, *95*, 4960.
(40) Bowman, J. M.; Schnider, H. M. *J. Chem. Phys.* **1999**, *110*, 4428.
(41) Gray, S. K.; Balint-Kurti, G. G.; Schatz, G. C.; Lin, J. J.; Liu, X.; Harich, S.; Yang, X. *J. Chem. Phys.* **2000**, *113*, 7330.
(42) Vibók, Á.; Balint-Kurti, G. G. *J. Chem. Phys.* **1992**, *96*, 7615.
(43) Vibók, Á.; Balint-Kurti, G. G. J. *J. Phys. Chem.* **1992**, *96*, 8712.
(44) Lill, J. V.; Parker, G. A.; Light, J. C. *Chem. Phys. Lett.* **1982**, *89*, 483.
(45) Lill, J. V.; Parker, G. A.; Light, J. C. *J. Chem. Phys.* **1986**, *85*, 900.